Journal of Materials Processing Technology 211 (2011) 57–65

Contents lists available at ScienceDirect

Journal of Materials Processing Technology

journal homepage: www.elsevier.com/locate/jmatprotec

A simple Eulerian thermomechanical modeling of friction stir welding

D. Jacquin[a], B. de Meester[b], A. Simar[b], D. Deloison[c], F. Montheillet[a], C. Desrayaud[a,*]

[a] Ecole des Mines de Saint-Etienne (Centre SMS), CNRS UMR 5146, 158, Cours Fauriel, 42023 Saint-Etienne, France
[b] Université Catholique de Louvain, iMMC, Louvain-la-Neuve, Belgium
[c] EADS, IW12, Suresnes, France

ARTICLE INFO

Article history:
Received 28 April 2010
Received in revised form 19 August 2010
Accepted 23 August 2010

Keywords:
Friction stir welding
Process model
Simple thermomechanical model

ABSTRACT

A simple three-dimensional thermomechanical model for friction stir welding (FSW) is presented. It is developed from the model proposed by Heurtier et al. (2006) based on a combination of fluid mechanics numerical and analytical velocity fields. Those velocity fields are introduced in a steady state thermal calculation to compute the temperature field during welding. They allow partial sliding between the shoulder and the workpiece, the amount of which is provided as an additional result of the model. The thermal calculation accounts for conduction and convection effects by means of the particular derivative. The complete thermomechanical history of the material during the process can then be accessed by temperature and strain rate contours.

The numerical results are compared with a set of experimental test cases carried out on an instrumented laboratory device. The choices for modeling assumptions, especially tribological aspects, are discussed according to agreements or deviations observed between experimental and numerical results. The amount of sliding appears to be significantly influenced by the welding conditions (welding and tool rotational velocities), and physical interpretations are proposed for its evolution.
© 2010 Elsevier B.V. All rights reserved.

1. Introduction

Friction stir welding (FSW) is a solid state joining process, which is particularly adapted for difficult-to-weld high strength aluminum alloys (e.g. the 2XXX and 7XXX series). Thomas et al. (1991) from The Welding Institute, TWI, patented the FSW process. A hard cylindrical tool with a threaded pin and a shoulder rotates and slowly plunges into the joint line between two workpieces butted together. Friction and stirring generate heat dissipation so that the metal pieces do not reach their melting point. The material is plastically deformed and transferred from the leading edge to the trailing edge of the tool, leaving a solid phase bond between the two pieces when the tool is moved along the joint line.

The control and the optimization of the process require the development of thermomechanical models for various aims. Complete understanding and mechanical optimization of the process may require fully thermomechanically coupled models ideally able to predict defects occurrence and/or residual stresses. By contrast, simple descriptions of the temperature field may be suitable to estimate the thermomechanical cycle to which elements of the material are subjected during the process. These histories can then be used for optimizing the weld through physical modeling of the microstructure evolution and consequent weld strength computed as post-processing.

Two types of process modeling techniques are reported: fluid dynamics and solid mechanics simulations. Ulysse (2002), Colegrove and Shercliff (2005), Feulvarch et al. (2005) performed 3-dimensional fluid dynamics simulations. Both formulations lead to strongly non-linear systems. Colegrove and Shercliff (2005) account for the tool threads contrarily to the early model by Ulysse (2002). Schmidt and Hattel (2006), Zhang et al. (2007), Zhang (2008), Zhang and Zhang (2009) and Guerdoux and Fourment (2009) reported solid mechanics models using the adaptive arbitrary Lagrangian–Eulerian (ALE) formulation. These very complete models of the process can predict the role played by the tool plunge depth on the formation of flashes, voids or tunnel defects and the influence of threads on the material flow, temperature field and welding forces.

Both solid and fluid modeling techniques involve non-linear phenomena belonging to the three classic types: geometric, material or contact nonlinearity. Furthermore, the high gradient values of the state variables near to the probe and the thermomechanical coupling imply a large number of degrees of freedom in FSW modeling, which is costly in CPU time: many hours calculations are classically required for one test case convergence.

Simplifications of the thermomechanical modeling of the process are suggested in the literature. Seidel and Reynolds (2003) use a 2D fluid model to understand the planar flow around the

* Corresponding author. Tel.: +33 4 77 42 00 14; fax: +33 4 77 42 66 78.
E-mail address: cdesrayaud@emse.fr (C. Desrayaud).

0924-0136/$ – see front matter © 2010 Elsevier B.V. All rights reserved.
doi:10.1016/j.jmatprotec.2010.08.016

pin. Schmidt and Hattel (2005) and Heurtier et al. (2006) use a prescribed velocity field to predict the effect of material convection on the temperature field. Zhang et al. (2007) developed a solid formulation in which the temperature field was obtained through local measurements and reconstituted in 3 dimensions. Hence, the remaining variables to be solved in the problem are displacement increments and thus a decrease in degree of freedom is achieved. The effect on computation time is however limited since the flow rule is a strongly non-linear function of the temperature. Bastier et al. (2008) developed a two-step simulation of the FSW process. The first step is a fluid dynamics 3D finite element model to establish the material flow and temperature field and the second step uses a solid mechanics model and the temperature field, material flow and precipitate dissolution predicted at the first step to estimate the residual stresses after welding.

Various models are available for the contact boundary conditions. Colegrove and Shercliff (2005) assume that the material is completely sticking to the tool. Schmidt and Hattel (2005) study the effect of sticking vs sliding or partially sticking conditions at the tool/workpiece interface on the temperature field. Heurtier et al. (2006), Bastier et al. (2008) and Ulysse (2002) distinguish between the contact with the shoulder considered as sticking or partially sliding and the contact with the pin that is assumed to be perfectly sliding circumferentially. Schmidt and Hattel (2006) found that a non-uniform contact condition is present at the tool/workpiece contact interface with closer to sticking conditions at the majority of the interface except close to the vicinity of the tool shoulder periphery and at the lower trailing advancing region of the pin/workpiece interface. A consequence of the material sliding at the tool/workpiece interface is the presence of a vertical velocity, accounting for the dragging of the metal by the thread of the pin, equal to the product of the tool rotational velocity $\dot{\Omega}_{\mathrm{tool}}$ [rad s^{-1}] and the thread pitch, i.e. $u_z = \dot{\Omega}_{\mathrm{tool}} \cdot L_f/2\pi$ see Colligan, 1999. Sliding contacts can be treated by introducing a contact law, increasing consequently the degrees of freedom of the problem. Dependence of the shear stress τ on the von Mises equivalent stress $\bar{\sigma}$ ($\tau \le \bar{m}(\bar{\sigma}/\sqrt{3})$ for the Tresca model, see Jacquin et al., 2007), or on the relative velocity of contacting surfaces Δv^p ($\tau = \alpha \cdot \Delta v^p$), or contact pressure P ($\tau \le \mu P$ for the Coulomb model) can be established ($\bar{m}$, α and μ are various friction coefficients). Solid models are more suitable for contact control in particular for switching between sticking and sliding conditions. Zhang et al. (2005) and Zhang et al. (2007) use a Coulomb limited by Tresca friction model in their 2-dimensional thermomechanical finite element model based on the ALE formulation. Zhang (2008) carried out comparisons on various models and showed that the Coulomb model could be used for friction stir welding at low rotational speeds.

This paper presents a model based on an Eulerian fluid thermal calculation, the convection term of which uses the velocity fields proposed by Heurtier et al. (2006) to describe the material flow around the tool. The power dissipated through plastic straining is estimated by means of a strain rate and temperature dependent flow rule including a strong nonlinearity with respect to the temperature variable. Assuming the velocity fields established by Heurtier et al. (2006) are suitable to describe the bulk material flow around the probe (and to account for boundary conditions), the decrease in the number of degrees of freedom in this model is three times larger than that obtained by Zhang et al. (2007).

2. Thermomechanical model

2.1. Kinematic assumptions

As mentioned above, the present model derives from the formulation proposed by Heurtier et al. (2006) to describe the material flow around the tool during the welding operation. The welding zone is divided into three parts (Fig. 1) defined as the flow arm zone (1) for the torsion velocity field, the stirring zone (2) for the "vortex like" velocity field, and the rest of the sheet (3). All three zones undergo the circumventive velocity field.

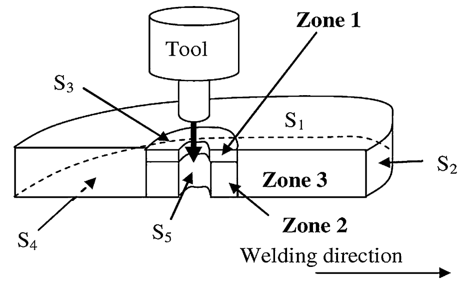

Fig. 1. Partition of the welding zone for the definition of the elementary velocity fields and boundaries of the model.

2.1.1. Circumventive velocity field

The classical circumventive two-dimensional velocity field defined for perfect fluids is used in zones 1, 2, and 3 of Fig. 1. This field describes material flow around the pin like water around a bridge pile. This field is defined in Eq. (1):

$$\vec{V} = \begin{bmatrix} u_r = v_\infty \left(1 - \dfrac{r_0^2}{r^2}\right) \cos\theta \\ u_\theta = -v_\infty \left(1 + \dfrac{r_0^2}{r^2}\right) \sin\theta - \dfrac{\Gamma}{2\pi r} \\ u_z = 0 \end{bmatrix} \tag{1}$$

where r_0 is the pin radius, r is the distance to the tool axis, Γ (m^2 s^{-1}) is the material circulation and v_∞ (m s^{-1}) is the welding velocity. The material circulation Γ is added to account for partial circumferential dragging of the material due to the rotation of the tool. $\Gamma/2\pi {r_0}^2$ is the angular velocity (s^{-1}) of the material dragged by the pin surface. It is assumed constant in the present model. As shown in Fig. 2, this term causes the dissymmetry between the advancing and retreating sides of the weld. The material does not completely stick to the pin, i.e. $\Gamma/2\pi {r_0}^2 \le \dot{\Omega}_{\mathrm{tool}}$, where $\dot{\Omega}_{\mathrm{tool}}$ (s^{-1}) is the rotational velocity of the tool. Based on our experimental measurements of the temperature distribution for three test cases, $\Gamma/2\pi {r_0}^2$ is set equal to $0.02\dot{\Omega}_{\mathrm{tool}}$ for all welding conditions. Note that this value of the sliding ratio is slightly low compared to the $0.1 \ldots 0.3\dot{\Omega}_{\mathrm{tool}}$ measured by Schmidt et al. (2006) by metallography as well as X-ray and computer tomography for similar welding conditions. When r tends to infinity the circumferential dragging velocity vanishes.

2.1.2. Torsion velocity field

Since friction occurs between the shoulder of the tool and the upper surface of the workpiece, it develops a shear strain under the surface. Therefore, a torsion velocity field (centred on the probe axis) is introduced to describe this shearing effect in the flow arm zone (zone 1 in Fig. 1). Its depth is limited to 1/5th of the sheet thickness as suggested by Heurtier et al. (2006), i.e. between z_{flowarm} and z_{surf}:

$$\vec{V} = \begin{bmatrix} u_r = 0 \\ u_\theta = r\dot{\Omega}_{\mathrm{surf}} \dfrac{z - z_{\mathrm{flowarm}}}{z_{\mathrm{surf}} - z_{\mathrm{flowarm}}} \\ u_z = 0 \end{bmatrix} \tag{2}$$

where the angular velocity $\dot{\Omega}_{\mathrm{surf}}$ [rad s^{-1}] is the rotational velocity of the workpiece surface. $\dot{\Omega}_{\mathrm{surf}}$ is lower than the tool rotational velocity $\dot{\Omega}_{\mathrm{tool}}$ because relative sliding is allowed. Finally, $\dot{\Omega}_{\mathrm{surf}}$ and $\dot{\Omega}_{\mathrm{tool}}$ are related by the contact algorithm described in Section 2.3.

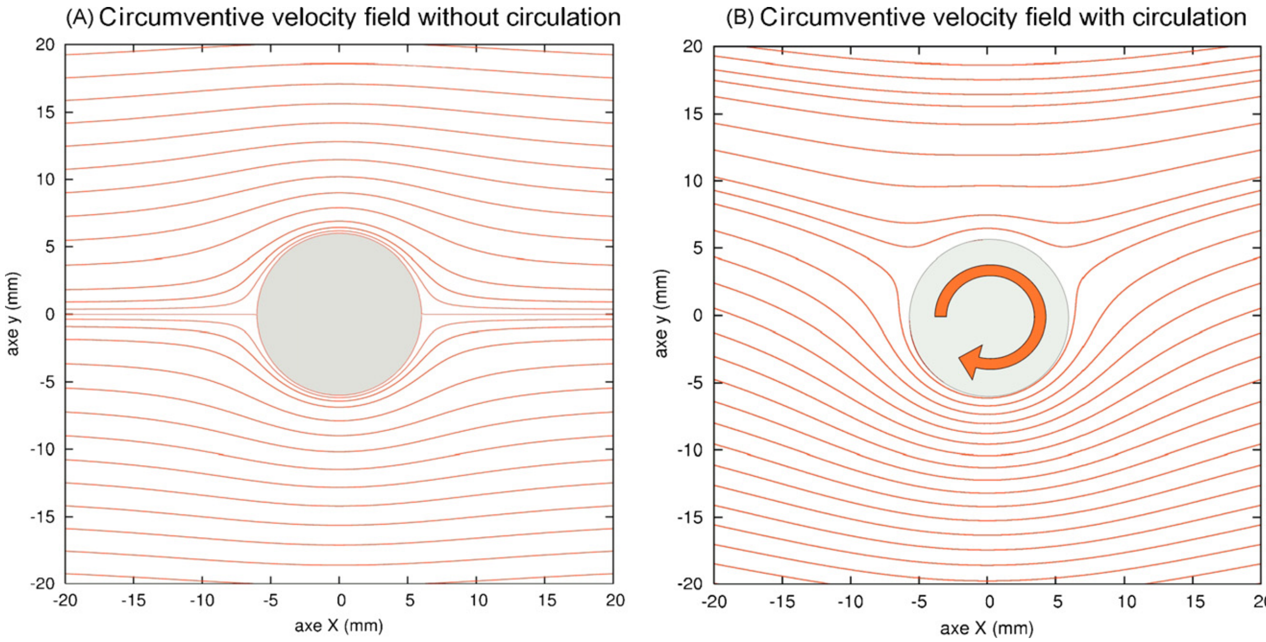

Fig. 2. Influence of the circulation intensity on the aspect of the flow lines.

The torsion velocity field is activated between $r = r_0$ and $r = r_s$, where r_s is the shoulder radius. To insure continuity in the velocity field, the circumferential component of the torsion velocity field (i.e. u_θ) is decreased linearly to zero in a transition zone between $r = r_s$ and $r = r_s + \Delta r$. The influence of Δr on the temperature field is found to be negligible. In the present model, it is set to 0.2 mm.

2.1.3. Vortex like velocity field

The partial sliding at the tool interface generates a vertical motion of the material dragged vertically by the thread of the pin. The vertical motion is described in a third component of the global velocity field: the vortex like velocity field in zone 2 of Fig. 1. Since the circumferential dragging by the pin is assumed low (i.e. $0.02\dot{\Omega}_{tool}$), the vertical dragging intensity is high.

The vortex like velocity field was already introduced by Heurtier et al. (2006) and assimilated to a vortex. Its description is improved in the present work through an accurate axisymmetric FEM calculation. The improvement is significant close to the pin where velocity gradients are high. The boundary conditions of the axisymmetric FEM calculation includes the vertical dragging of the material by the thread of the pin (see Fig. 3), the maximal intensity of which equals to the thread pitch multiplied by the tool rotational velocity. It corresponds to the case where complete circumferential sliding of the pin relative to the material occurs. As a partial circumferential dragging of the material around the probe occurs (described by the parameter Γ), the vertical dragging velocity takes the following form: $u_z = (\dot{\Omega}_{tool}/2\pi - \Gamma/4\pi^2 r_0^2)L_f$. Where L_f is the pitch of the pin thread. Note that if the material is sticking to the pin then $\Gamma/2\pi r_0^2 = \dot{\Omega}_{tool}$, and hence no vertical dragging occurs (i.e. $u_z = 0$). This balance between circumferential sliding and vertical dragging (screwing effect of the pin thread) is formally included in the present model in which the sliding ratio of the material around the pin is imposed as suggested by Heurtier et al. (2006), Bastier et al. (2008) and Ulysse (2002).

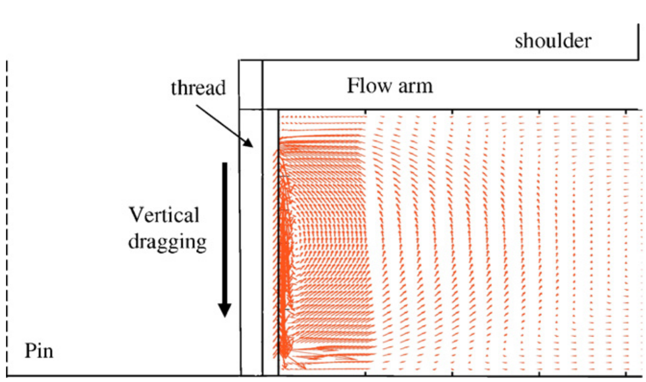

Fig. 3. Vortex velocity field in an axisymmetric (r–z) plane.

Fig. 3 features the vortex like velocity field in the vicinity of the pin inside the workpiece, i.e. in zone 2 of Fig. 1. The velocity field in Fig. 3 is obtained by means of an isothermal calculation involving a material following a Norton-Hoff law with an exponent m equal to 0.12. Far from the pin, the vortex intensity vanishes (for $r = r_s$) as expected in the material not affected by welding. At the top of the vortex zone (zone 2 in Fig. 1), all components of the torsion velocity field (Eq. (2) with $z = z_{flowarm}$) and all components of the vortex like velocity field are equal to zero resulting in a perfect continuity of these two velocity fields at the interface between zone 1 and 2 of Fig. 1.

2.1.4. Global velocity field

Addition of these three elementary velocity fields approximates the material flow during friction stir welding. The circumventive velocity field applies everywhere in the model. The torsion velocity field and vortex like velocity field apply respectively in zone 1 and in zone 2 of Fig. 1. Far from the pin, every component of the global velocity field vanishes, except the welding velocity v_∞. The global velocity field assumes incompressibility like each velocity field composing it. Flow lines can be integrated directly from this global velocity field by a first order Eulerian method. The above velocity field depends on four parameters: v_∞, $\dot{\Omega}_{tool}$, $\dot{\Omega}_{surf}$ and Γ.

2.2. Thermal calculation

The thermal calculation is carried out over the volume of the metal sheet. The tool and the clamping system are represented through boundary conditions on various surfaces. An Eulerian steady state formulation is chosen resulting in the following energy balance:

$$\mathrm{div}(\lambda \cdot \vec{\nabla} T) + \Gamma_{\mathrm{d}} \cdot K \cdot \mathrm{e}^{mQ/RT} \cdot \dot{\bar{\varepsilon}}^{m+1} = \rho \cdot c \cdot \vec{v} \cdot \vec{\nabla} T \tag{3}$$

where λ is the thermal conductivity [$\mathrm{W\,m^{-1}\,K^{-1}}$], T is the temperature [K], $\Gamma_{\mathrm{d}} = 0.92$ is the Taylor–Quinney parameter accounting for the fact that a small part of the energy is stored in the material in the form of defects, K is the "viscosity like" parameter [$\mathrm{MPa\,s}^m$], m is the strain rate sensitivity, Q is the activation energy of the material flow [$\mathrm{kJ\,mol^{-1}}$], $\dot{\bar{\varepsilon}}$ is the equivalent von Mises plastic strain rate, ρ is the material density [$\mathrm{kg\,m^{-3}}$] and c is the specific heat [$\mathrm{J\,kg^{-1}\,K^{-1}}$]. The particular derivative term (right hand term) and the strain rate (second left hand term) are calculated through the global velocity field $\vec{V}$ describing the material flow around the tool, see Section 2.1.

The flow stress σ_0 is assumed to be equal to a power viscoplastic Arrhénius law, with non-linear strain rate sensitivity.

$$\sigma_0 = K\dot{\bar{\varepsilon}}^{m}\,\mathrm{e}^{mQ/RT} \tag{4}$$

2.3. Boundary conditions

2.3.1. Thermal boundary conditions

Fig. 1 also defines the surfaces of the model represented by a hollow cylinder where the internal surface corresponds to the tool pin. The bottom of the cylinder S_4 is set on the backing bar and its upper surface S_1 stands in air at room temperature. The boundary condition on the external side surface S_2 is also defined by an exchange coefficient across the surface, similarly to the boundary conditions on all other surfaces (except on S_3 where friction occurs):

$$\lambda \frac{\partial T}{\partial \vec{n}_i} = H_i(T_i - T_i^{\mathrm{sink}}) \tag{5}$$

where $\vec{n}_i$ is normal to the surface i, H_i is an exchange coefficient across the surface i bathing in a fluid at a sink temperature far from the surface T_i^{sink}. The selected numerical values for the exchange coefficients are as follows: $H_1 = 30\,\mathrm{W\,m^{-2}\,{}^{\circ}C^{-1}}$ (air cooling) and the sink temperature is set to 20 °C, $H_4 = 200\,\mathrm{W\,m^{-2}\,{}^{\circ}C^{-1}}$ and the sink temperature in the backing bar is set to 100 °C according to the value optimized by Feulvarch et al. (2005). After various tests on the model, the value of $H_2 = 400\,\mathrm{W\,m^{-2}\,{}^{\circ}C^{-1}}$ was set. Numerical experiments have shown that when the size of the model is large enough the influence of the selected value for this parameter on the final results is small.

2.3.2. Mechanical boundary conditions

The mechanical boundary conditions are introduced in the definition of the global velocity field, accounting for sliding phenomena between the tool shoulder and the metal sheet. As discussed in Section 2.1, the present model allows a certain amount of sliding between the tool shoulder and the welded metal as suggested by Schmidt et al. (2006) and Zhang and Zhang (2009). At the opposite of the model proposed by Zhang and Zhang (2009), the contact equilibrium is not solved locally in the present model but the amount of global shoulder sliding is one of the results. The velocity discontinuity generated by this sliding phenomenon implies a surface power dissipation $\dot{W}_{\mathrm{surf}}$ given by:

$$\dot{W}_{\mathrm{surf}} = \frac{\bar{m}}{\sqrt{3}}\sigma_0 \dot{\Omega}_{\mathrm{sliding}} \tag{6}$$

if the Tresca formulation is chosen for the contact stress. The value chosen for the friction coefficient is $\bar{m} = 0.45$. For any point of the tool shoulder surface S_3 located at a distance r from the probe axis, the sliding velocity is $\dot{\Omega}_{\mathrm{sliding}} = \dot{\Omega}_{\mathrm{tool}} - \dot{\Omega}_{\mathrm{surf}}$. The velocity of the material at the tool/workpiece interface in the flow arm zone (zone 1 in Fig. 1) $\dot{\Omega}_{\mathrm{surf}}$, is calculated as follows: we define the mean radius in the welded zone as $r_{\mathrm{m}} = r_{\mathrm{s}} + r_0/2$ where r_{s} and r_0 are respectively the shoulder and pin radius. At each iteration, the mean value of equivalent stress and temperature (at $r = r_{\mathrm{m}}$) are used to calculate the mean strain rate $\dot{\bar{\varepsilon}}_{\mathrm{m}}$ in the vicinity of the probe by reversing the flow rule (Eqs. (4) and (6)). Assuming that only shear strain occurs between the surface (where $\dot{\Omega} = \dot{\Omega}_{\mathrm{surf}}$) and the bottom of the metal sheet (where $\dot{\Omega} = 0$), the surface velocity can be expressed as

$$\dot{\Omega}_{\mathrm{surf}} = \frac{h\sqrt{3}\dot{\bar{\varepsilon}}_{\mathrm{m}}}{r_{\mathrm{m}}} \tag{7}$$

where h is the height of the flow arm zone 1 (see Fig. 1), $h = z_{\mathrm{surf}} - z_{\mathrm{flowarm}}$. The value of $\dot{\Omega}_{\mathrm{surf}}$ is hence finally found by iteration on the model as described in Section 3.

The power generated through tribologic effects in the shoulder contact is distributed between the tool and the welded material based on their relative effusivities. The computation shows that about 70% of the surface power density is transferred into the bulk of the workpiece.

3. Numerical implementation

The procedure to solve the problem is as follows. At the beginning of the simulation the temperature is set on the entire mesh at 20 °C. The global velocity field is prescribed by the welding and the tool rotational velocities (see Eqs. (1) and (2) and Section 2.1) as well as $\dot{\Omega}_{\mathrm{surf}}$. At the first iteration, this sliding ratio is set equal to 10% of the tool rotational velocity such that $\dot{\Omega}_{\mathrm{surf}} = 0.1\dot{\Omega}_{\mathrm{tool}}$. Eq. (3) must then be solved. The mechanical aspects of the problem are included in the thermal balance Eq. (3) by means of the particular derivative term (accounting for the global velocity field at each position of the welded zone). The second term concerning the volume dissipated power density $\dot{W}_{\mathrm{vol}} = \Gamma_{\mathrm{d}}\sigma_0\dot{\bar{\varepsilon}}$ is accounting for the rheology of the welded material (Eq. (4)). Eq. (4) must be linearized in the vicinity of the temperature at the preceding iteration. The surface power $\dot{W}_{\mathrm{surf}}$ introduced into the material at the contact with the tool shoulder is calculated based on Eqs. (4) and (6). After solving Eq. (3) on the entire mesh, providing the new temperature distribution, the new value of $\dot{\Omega}_{\mathrm{surf}}$ is calculated on the basis of Eq. (7). It is then verified that friction heat power transferred into the welded zone (Eq. (6)) coincides with the surface power at the surface of the sheet contacting the shoulder calculated by integrating the temperature gradient at the tool interface. If the two surface powers are not close to identical, a new iteration is performed. The system is auto-regulated and both surface powers are found identical after only a few iterations, i.e. the successive values of $\dot{\Omega}_{\mathrm{surf}}$ stabilize at a constant value.

A cylindrical coordinate system is chosen for the hollow cylinder and regular intervals are defined along the r, θ and z axes, i.e. Δr, $\Delta\theta$ and Δz, respectively. The first and second gradients of the temperature are linearized. The mesh structure is represented in Fig. 4.

The system is solved through a classic Newton–Raphson method, written in Fortran, actualizing the temperature and the sliding ratio at each iteration. An additional Fortran procedure was written to plot and treat the results in the Abaqus™ environment (CAE). Abaqus CAE is used since it can post-treat and display very large result files assuming they are provided in the correct format.

4. Material and experimental procedure

4.1. Material data

The base material of the present study is a AA2024 sheet, rolled down to 3.2 mm and welded in the T351 temper state (i.e. quenched and tensioned 0.5–2%, then maturated at room temperature). Table 1 gives the chemical composition of the alloy.

According to Mills (2002), the thermal properties are as follows: the average value of the thermal conductivity $\lambda = 130\,\mathrm{W\,m^{-1}\,K^{-1}}$, density $\rho = 2700\,\mathrm{kg\,m^{-3}}$, and specific heat $c = 850\,\mathrm{J\,kg^{-1}\,K^{-1}}$.

Table 1
Composition of the AA2024 base material.

Comp %	Si	Fe	Cu	Mn	Mg	Cr	Zn	Ti	Zr
AA2024	0.087	0.19	4.1	0.5	1.4	0.015	–	0.01	58 ppm

Table 2
Characteristics of the welding tool.

Tilt angle	Pin diameter	Pin height	Pin shape	Shoulder shape	Shoulder diameter	Tool material
0°	5 mm	2.9 mm	Cylindrical, threaded M5, flat pin end	Scrolled	15 mm	Z40CDV 5.1 hardened to 50 HRC

The bulk material behaviour is assumed to follow a power law given by Eq. (4). The involved parameters were measured by hot torsion testing on a 5 mm thick metal sheet: the "viscosity like" parameter K is equal to 1.5 MPa s^m, the strain rate sensitivity m is equal to 0.12, and the activation energy Q is equal to 155 kJ mol^{-1}.

4.2. Experimental procedure

Welding experiments were performed at UCL using a HERMLE 3-axis CNC milling machine (UWF 1001 H) under control of displacement. The 3.2 mm thick plates were 70 mm wide and 600 mm long. They were firmly clamped onto a 80 mm thick, 450 mm wide and 630 mm long steel backing plate. The welds were 500 mm long and always parallel to the rolling direction. The characteristics of the tool are given in Table 2.

Type K Thermo-Electric MTS-56050 thermocouples (0.5 mm diameter) were embedded into the workpiece on the advancing and retreating sides and within the backing plate by drilling 1.0 mm diameter holes and using conducting pasta in the hole. These thermocouples were located along the weld axis with a 10 mm spacing along the welding direction, at 8.9, 10, 12, 14 and 16 mm from the weld axis, respectively on both sides of the weld at mid-thickness. Torque measurement is performed by means of a piezoelectric 3D sensor (Kistler 912 4A). Hence, the total power dissipated during welding can be estimated by multiplying the measured torque by the tool rotational velocity (expressed in s^{-1}).

Three validation test cases were fully instrumented for temperature measurements with the following welding parameters:

– test case 1: 400 rpm, 400 mm/min (advance per revolution = 1);
– test case 2: 800 rpm, 400 mm/min (advance per revolution = 0.5);
– test case 3: 400 rpm, 100 mm/min (advance per revolution = 0.25).

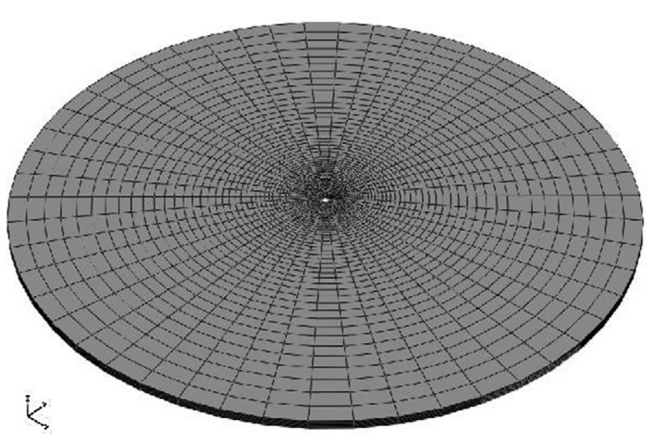

Fig. 4. schematic aspect of the mesh for the finite difference simulations.

These cases will be referred to as being respectively cold (1), intermediate (2) and warm (3) welding test cases. Comments on these definitions will be brought in Section 5. Five additional welds were performed with torque measurements in order to provide a good overview of the model accuracy in terms of dissipated power. Operating parameters for these additional test cases can be found in Fig. 9.

5. Results and discussion

5.1. Simulation results

Numerical tests were performed to reveal the effect of the welding parameters on the temperature in the vicinity of the tool. Table 3 summarizes all the cases considered for modeling.

Fig. 5 shows the aspect of the temperature contours obtained when setting the tool rotational velocity to 400 rpm and increasing the welding velocity from 100 mm/min up to 800 mm/min. A test case is calculated on a personal computer in about 1 h.

The convection effect rate through the meshed volume due to the tool translation is increasing when the welding velocity increases and generates cooling due to the transport of cold material towards the tool. The maximum and minimum temperature values in the meshed zone are shown in Fig. 6.

The minimum value is always observed ahead of the tool while the maximum is observed close to the tool shoulder. For the warmer test cases, the maximum temperature value are found to be slightly higher than the solidus temperature (equal to 525 °C for the AA2024). This may explain the local defects (or flashes) observed for the test cases 2 and 3. However, the excursions over 525 °C are very short (few seconds) in these test cases, minimizing thus the negative impact on the welded material properties. For the test case

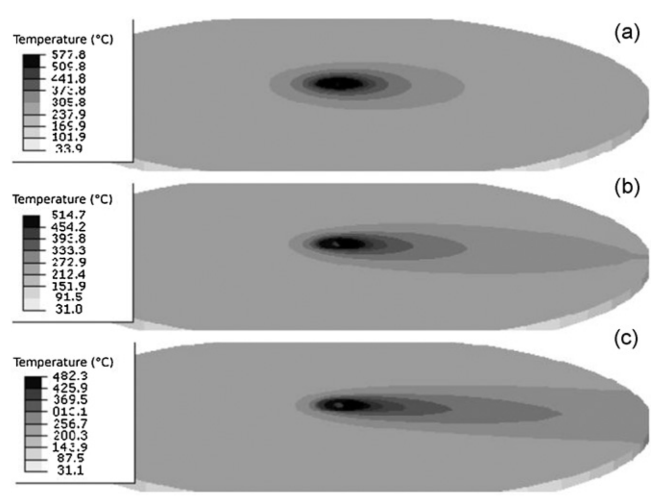

Fig. 5. Temperature contours obtained for a tool rotational velocity equal to 400 rpm, for welding velocities of the tool equal to (a) 100 mm/min, (b) 400 mm/min and (c) 800 mm/min.

Table 3
Summary of the welding conditions for the numerical test cases considered.

	V_t = 100 mm/min	V_t = 200 mm/min	V_t = 300 mm/min	V_t = 400 mm/min	V_t = 600 mm/min	V_t = 800 mm/min
V_r = 50 rpm				*		
V_r = 200 rpm			*	*		
V_r = 300 rpm			*	*		
V_r = 400 rpm	*	*	*	*	*	*
V_r = 600 rpm			*	*		
V_r = 800 rpm	*	*	*	*		

1, the maximum temperature is found under 525 °C. Test case 1 is thus considered as a cold welding condition. Hence, the predictions of the model seem relevant.

As expected in friction stir welding, the maximum temperature value decreases when the welding velocity increases. This is due to the heat convected by the material flow: the higher the welding velocity, the lower the temperature in the vicinity of the tool. The maximum temperature increases with the tool rotational velocity. By contrast, the minimum temperature is weakly affected by the tool rotational velocity. This illustrates the fact that the size of the model is large enough.

5.2. Comparison with experiments

5.2.1. Test case 1

Calculated and measured thermal histories are shown in Fig. 7 for all the thermocouples on the advancing and retreating sides of the weld. For clarity, the calculated thermocouple histories are shifted by 10 s towards negative times with respect to the experimental plots.

The general comparison of the experimental and calculated thermocouples records indicates rather good agreement, even if the advancing side temperature values are underestimated and the retreating side values overestimated by the model (see Fig. 7). The qualitative temperature dissymmetry between advancing and retreating side is correctly reproduced by the model, due to the existence of a circulation component in the circumventive velocity field described in Section 2.1.

For the test cases 2 and 3, the temperature comparisons are made through the peak temperatures at two thermocouples locations (see Fig. 8).

5.2.2. Test case 2

The test case 2 was expected to be an intermediate temperature weld case. Indeed, it is found to be somewhat warmer on average than test case 1 (see Fig. 8) due to the larger tool rotational velocity. The partition between the frictional power and the plastic power predicted by the model is modified compared to test case 1. In test case 2, the sliding ratio (78%) is founded much higher than in test case 1 (56%). Thus, the sliding ratio increases with the tool rotational velocity. Consequently, on the one hand the effective velocity of the material contacting the shoulder appears to be somewhat lower in case 2 than in case 1, on the other hand the frictional power in case 2 is much higher than in case 1 due to the high value of the sliding ratio resulting in larger temperatures in test case 2 compared to test case 1.

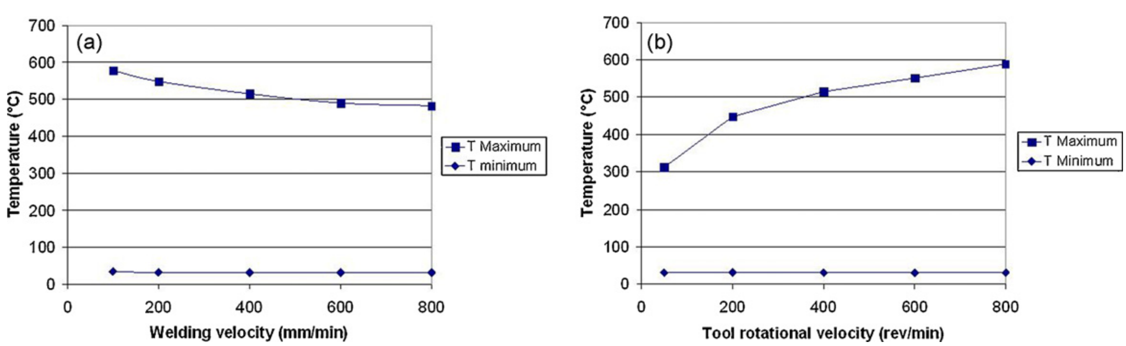

Fig. 6. Extreme temperatures in the welds (a) as a function of the welding velocity of the tool for a tool rotational velocity equal to 400 rpm and (b) as a function of the tool rotational velocity for a welding velocity equal to 400 mm/min.

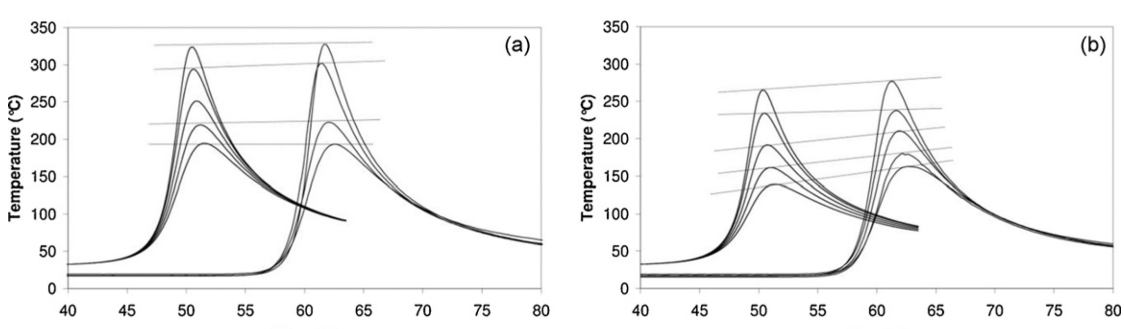

Fig. 7. Comparison between measured and calculated temperature cycles at the thermocouple locations in test case 1 on (a) the advancing side and (b) the retreating side. The calculated cycles are shifted by 10 s towards negative times with respects to the experimental plots for better lisibility. Note that one temperature measurement was unavailable.

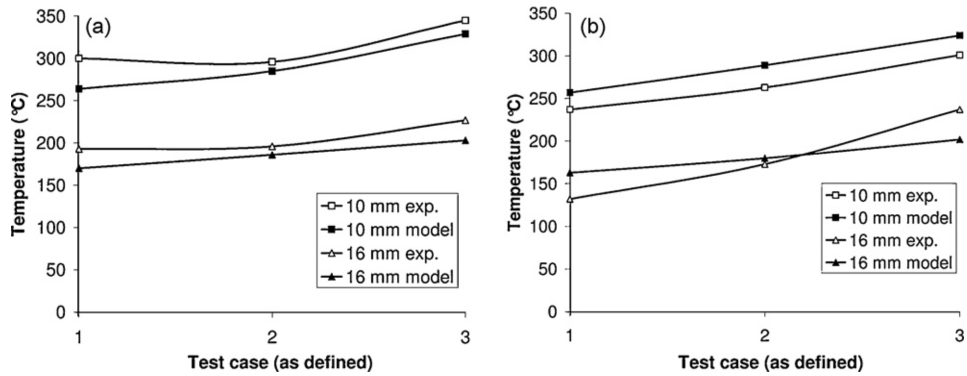

Fig. 8. Comparison of measured and predicted peak temperatures at 10 and 16 mm away from the weld line for test case 1 (cold weld), 2 (intermediate temperature) and 3 (hot weld) on (a) the advancing side and (b) the retreating side of the weld.

5.2.3. Test case 3

As expected, this test case appears as a warm welding case. The predicted and measured temperatures on Fig. 8 are indeed higher than in the two former cases. These results evidence the efficiency of the Eulerian formulation employed in the present model, in which the average temperature increases significantly when decreasing the welding velocity. In the present case the sliding ratio is found much lower than for test case 1 (i.e. 10%) indicating that the metal is intensively dragged by the shoulder of the tool.

5.3. Power balance and evolution of the sliding ratio

More than the temperature history and contours, the present model provides data on the power and especially on the partition of the latter between the plastic (volume) and surface dissipation contributions. The plastic power considered in this model is composed of the plastic dissipation in the depth of the sheet and in the subsurface shear layer in the flow arm zone due to the torsion velocity field.

This partition is made through the estimation of the sliding ratio in the contact between the tool and the metal sheet surface. An accurate analysis of this output of the model is proposed here as a synthesis of the model relevance. Fig. 9 compares the predicted and measured evolution of the power dissipated in the weld as a function of the welding parameters. The plastic (volume) and surface parts of this power value are also presented.

In the present model, the sliding amount between the shoulder and the workpiece defines the power dissipated at the surface during welding. If complete sticking occurs between the shoulder and the workpiece, the calculated power dissipated at the surface is equal to zero, but a large plastic dissipation occurs in the flow arm (subsurface of the shoulder) contributing to a frictional power during welding.

Fig. 9(a) presents the partition of the power between the surface and plastic part as a function of the welding velocity. The increase of the total power with the welding velocity is verified experimentally. Similarly, Simar et al. (2006) concluded from their torque measurements on 6005A-T6 welds that the power increases

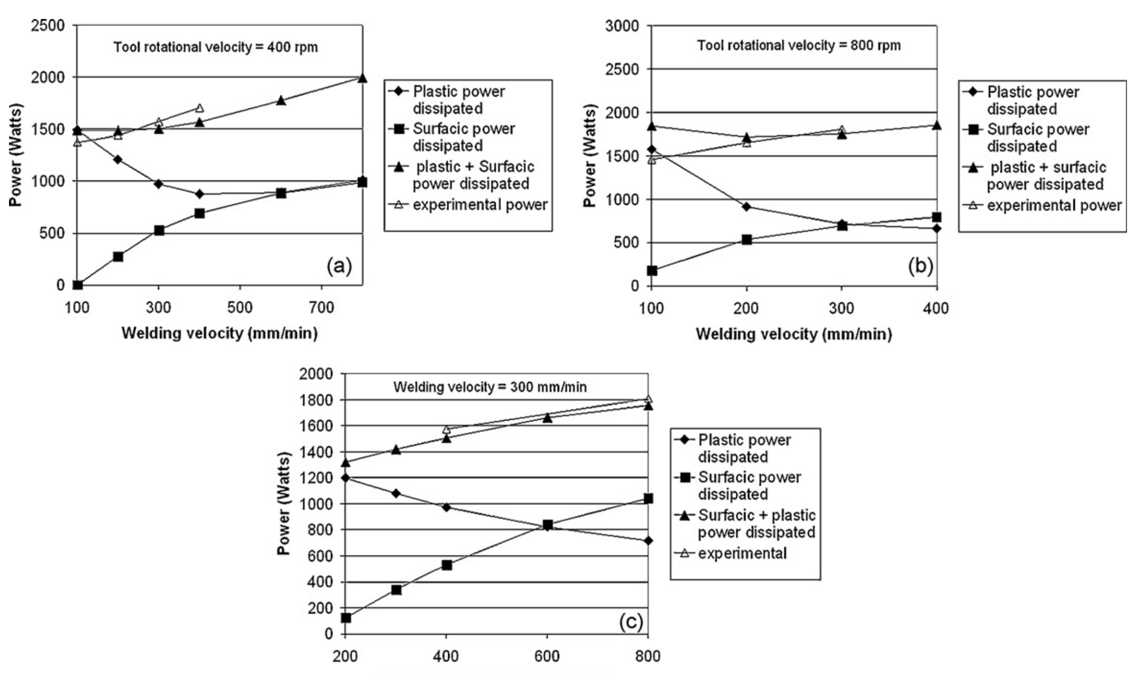

Fig. 9. Repartition of the predicted power dissipation in the weld between plastic power and surface power as a function of (a) and (b) the welding velocity and (c) the tool rotational velocity. Comparison with the measured torque converted in total power input, where available.

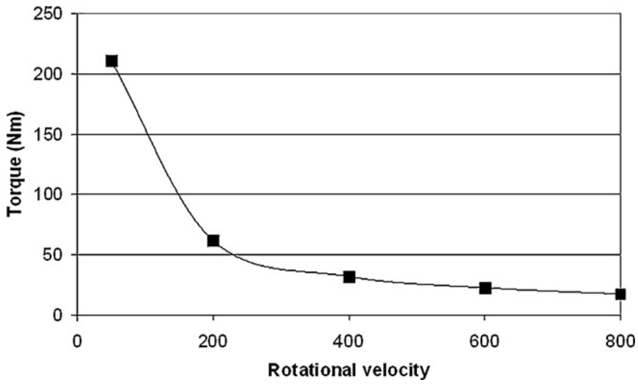

Fig. 10. Evolution of the predicted torque as a function of the tool rotational velocity for an advancing speed equal to 400 mm/min.

linearly with increasing welding velocity. Although the total power dissipated in the weld increases with the welding velocity, the maximum temperature value was shown to drop in Fig. 6. This effect can be explained by the Eulerian cooling flux which increases with the welding velocity. A significant part of the additional power generated when the welding velocity increases is in fact conveyed by the metal flux far from the weld, and thus not used to “overheat” the vicinity of the probe.

The partition of the total power into surface and plastic parts appears to change significantly with the welding velocity. As the latter increases, the temperature decreases in the vicinity of the probe and thus the sliding ratio increases due to the fact that the bulk material hardens at low temperatures (see Eq. (4)). Indeed, the hardening material cannot accommodate the large tool velocity any more. At the opposite, for the lower welding velocity, the material sticks completely to the shoulder. The velocity accommodation between the rotating tool and the backing bar implies intense shearing, especially in the subsurface of the shoulder generating an intense friction shear layer in the flow arm due to the torsion velocity field.

It is worth to note that the global power is accurately predicted in every test case excepted for the warmer test case, i.e. 800 rpm – 100 mm/min, see Fig. 9(b). Indeed, during welding a lot of “flashes” were generated near the tool and its aspect revealed local melting as expected according to the maximum temperature value calculated (over 630 °C). The present model is unable to capture the resulting loss of power, hence the overestimated total power found in Fig. 9(b) for that very warm test case.

The power increases with the tool rotational velocity (Fig. 9(c)). In the present case, where the welding velocity is kept constant, the power evolution can be related to the maximum temperature also increasing with the tool rotational velocity (see Fig. 6). Indeed, it is known experimentally that, if the tool rotational velocity is too high, flashes or local welding of the metal sheet may occur. The evolution of the power dissipated is the result of the partition between plastic powers and the power dissipated at the tool surface. The main part of the power appears to be plastic for the lower tool rotational velocity, due to the low value of the sliding ratio generating high torque values. At the opposite, the sliding ratio increases with the tool rotational velocity and thus the power dissipated at the tool surface becomes predominant with respect to plastic dissipation. The dependence of the torque on the tool rotational velocity is shown in Fig. 10. Yan et al. (2005) measured the torque during welding in AA2524-T351 and reported similar values and trends for the welding torque as a function of rotational velocity predicted by the present model and presented in Fig. 10.

6. Conclusions

A simplified thermomechanical model was developed for friction stir butt welds. Based on kinematically compatible assumptions, this model predicts temperature contours in the welded zone, power dissipation, and the sliding ratio on the interface between the shoulder and the workpiece. A successful comparison with experiments was carried out and the general tendencies for the influence of operational parameters were well predicted. The analysis of results concerning the contact conditions provides interesting data about the evolution of the relative sliding between the shoulder and the material to be welded. The sliding ratio increases with the tool rotational velocity and decreases with the temperature in the vicinity of the tool.

The control of the sliding ratio is of prime interest to optimize the stirring of the metals to weld and minimize the thermomechanical loading on the tools. If the sliding ratio is too small, complete sticking of aluminum can occur and thus increase drastically the torque (eventually leading to fracture). In contrast, if it is too high, local melting or flashes can appear and generate instabilities during welding.

Acknowledgements

The authors wish to thank the European community and the French National research Agency (ANR) for their financial support to the DEEPWELD and INNOFORM project in the context of which the work was performed. DEEPWELD (“Detailed Multi-Physics Modelling of Friction Stir Welding”, AST4-CT-2005-516134) is a 36-month Specific Targeted Research Project (STREP) co-funded by the 6th Framework Programme of the European Community. The project INNOFORM (INNOvative and Competitive FORMed Integral Structures Concepts) was funded by the 2006 call of the RNMP MATETPRO (ANR). A. Simar is a post-doctoral researcher of the FNRS, Belgium.

References

Bastier, A., Maitournam, M., Roger, F., Dang Van, K., 2008. Modelling of the residual state of friction stir welded plates. J. Mater. Process. Technol. 200, 25–37.
Colegrove, P.A., Shercliff, H.R., 2005. 3-Dimensional CFD modeling of flow round a threaded friction stir welding tool profile. J. Mater. Process. Technol. 169, 320–327.
Colligan, K., 1999. Material flow behavior during friction stir welding of aluminum. Welding J. 78 (7), 229–237.
Feulvarch, E., Boitout, F., Bergheau, J.M., 2005. Friction stir welding: Modélisation de l'écoulement de la matière pendant la phase de soudage. In: 17ème Congrès Français de Mécanique, Troyes.
Guerdoux, S., Fourment, L., 2009. A 3D numerical simulation of different phases of friction stir welding process. Mod. Simul. Mater. Sci. Eng. 17, 075001.
Heurtier, P., Jones, M.J., Desrayaud, C., Montheillet, F., Allehaux, D., Driver, J., 2006. Mechanical and thermal modeling of friction stir welding. J. Mater. Process. Technol. 172, 152–158.
Jacquin, D., Desrayaud, C., Montheillet, F., 2007. A thermo-fluid analysis of the friction stir welding process. Mater. Sci. Forum 539–543, 3832–3837.
Mills, K.C., 2002. Recommended Values of Thermophysical Properties for Selected Commercial Alloys. Woodhead Publishing Limited, Cambridge, UK.
Seidel, T.U., Reynolds, A.P., 2003. Two-dimensional friction stir welding process model based on fluid mechanics. Sci. Technol. Welding Joining 8, 175–183.
Schmidt, H., Hattel, J., 2005. Modelling heat flow around tool probe in friction stir welding. Sci. Technol. Welding Joining 10 (2), 176–186.
Schmidt, H., Hattel, J., 2006. Modelling themomechanical conditions at the tool/matrix interface in Friction Stir Welding. In: 5th Inter. Symp. FSW, Metz, France.
Schmidt, H.N.B., Dickerson, T.L., Hattel, J.H., 2006. Material flow in butt friction stir welds in AA2024-T3. Acta Mater. 54, 1199–1209.
Simar, A., Lecomte-Beckers, J., Pardoen, T., de Meester, B., 2006. Effect of boundary conditions and heat source distribution on temperature distribution in friction stir welding. Sci. Technol. Welding Joining 11 (2), 170–176.
Thomas, W.M., et al., 1991. Friction-stir butt welding. GB Patent No. 9125978.8, International patent application No. PCT/GB92/02203.

Ulysse, P., 2002. Three-dimensional modeling of the friction stir welding process. Int. J. Machine Tools Manufacture 42, 1549–1557.
Yan, J.H., Sutton, M.A., Reynolds, A.P., 2005. Process-structure-property relationships for nugget and heat affected zone regions of AA2524-T351 friction stir welds. Sci. Technol. Welding Joining 10 (6), 725–736.
Zhang, H.W., Zhang, Z., Chen, J.T., 2005. The finite element simulation of the friction stir welding process. Mater. Sci. Eng. A 403, 340–348.
Zhang, H.W., Zhang, Z., Chen, J.T., 2007. 3D modeling of material flow in friction stir welding under different process parameters. J. Mater. Process. Technol. 183, 62–70.
Zhang, Z., 2008. Comparison of two contact models in the simulation of friction stir welding process. J. Mater. Sci. 43 (17), 5867–5877.
Zhang, Z., Zhang, H.W., 2009. Numerical studies on controlling of process parameters in friction stir welding. J. Mater. Process. Technol. 209, 241–270.